Ferroelectrics

ISSN: (Print) (Online) Journal homepage: https://www.tandfonline.com/loi/gfer20

Synthesis, microstructure and magnetic properties of Co^{2+} and Al^{3+} substituted La-Zn nano ferrites

U. M. Mandle, L. A. Dhale, R. M. Tigote, K. S. Lohar & B. L. Shinde

To cite this article: U. M. Mandle, L. A. Dhale, R. M. Tigote, K. S. Lohar & B. L. Shinde (2021) Synthesis, microstructure and magnetic properties of Co^{2+} and Al^{3+} substituted La-Zn nano ferrites, Ferroelectrics, 584:1, 148-160, DOI: 10.1080/00150193.2021.1984766

To link to this article: https://doi.org/10.1080/00150193.2021.1984766

Published online: 08 Dec 2021.

FERROELECTRICS
2021, VOL. 584, 148–160
https://doi.org/10.1080/00150193.2021.1984766

Taylor & Francis
Taylor & Francis Group

Synthesis, microstructure and magnetic properties of Co^{2+} and Al^{3+} substituted La-Zn nano ferrites

U. M. Mandle[a], L. A. Dhale[b], R. M. Tigote[c], K. S. Lohar[b], and B. L. Shinde[d]

[a]Department of Chemistry, Sangmeshwar College, Solapur, MS, India; [b]Department of Chemistry, Shrikrishna Mahavidyalaya, Gunjoti, MS, India; [c]Department of Chemistry, Osmanabad Sub-Centre, Dr. Babasaheb Ambedkar Marathwada University, Aurangabad, MS, India; [d]Department of Chemistry, Waghire College, Saswad, MS, India

ABSTRACT
Co^{2+} and Al^{3+} substituted La-Zn ferrites synthesized by sol-gel auto-combustion method with glycine as a fuel, calcination temperature of samples confirmed from TGA analysis. The observed elemental analysis (EDAX) is in good agreement with the theoretical composition. The lattice constant decreases while the crystalline size increases with the increase in concentrations of dopant. Zn^{2+} ions prefer to occupy the tetrahedron site and other ions mainly enter octahedron site. The I.R. spectra have shown two principle absorption bands near 600 and 400 cm^{-1}. SEM and TEM images reveal well defined nanoparticles with slight agglomeration. Magneton number decreased with dopant substitution.

ARTICLE HISTORY
Received 22 April 2021
Accepted 4 August 2021

KEYWORDS
La-Zn ferrites; microstructure; lattice constant; saturation magnetization

1. Introduction

Ferrites are class magnetic iron oxides which plays an important role due to their extensive technological applications due to their both electrical and magnetic properties [1–3]. AB_2O_4 is a general chemical formula of spinel ferrite composed of tetrahedral-A and octahedral-B sites, where divalent-A^{2+}, trivalent-B^{3+} and oxygen ions form an fcc close packed structure. The distribution of these ions among A-sites and B-sites determines the characteristics of spinel ferrite [4].

Spinel ferrites are extensively used in applications such as sensor [5], catalysis [6, 7], biomedicine [8], MRI [9], drug delivery [10], magnetic recording [11], microwave devices [12] and magnetic ferro-fluids [13], etc. The structural, magnetic and electric properties of ferrites governed by many factors including substituents, preparation technique, elemental composition, processing temperature, particle size etc [14–16]. Numerous techniques been used for synthesis of nano-particles of ferrites are; hydrothermal [17], ball-milling [18], sol-gel auto-combustion [19], co-precipitation [15], reverse micelle [20], solid-state [21] etc. Amongst these techniques; the sol-gel auto combustion technique is facile, which is easy to control and produce the ferrite nanoparticle samples with the large surface area.

CONTACT B. L. Shinde shindebl1981@gmail.com

Among all the spinel ferrites, Co-Zn ferrites have attracted huge attention due to its high permeability as well as high saturation magnetization. Cobalt-substituted zinc ferrites are commonly known as magnetic ceramics. The electrical and magnetic properties of ferrites extensively altered by doping of trivalent ions like Al^{3+}, Cr^{3+}etc. for Fe^{3+} ion [22, 23].

Aluminum (Al^{3+}) substituted ferrites because of their low-eddy current losses, high electrical resistivity, high squareness magnetic hysteresis loop with moderate saturation magnetization, high chemical stability are capable for numerous technological applications over broad frequency range [24, 25]. Furthermore, ferrites with good electrical and magnetic characteristics can be attained by adding rare earth (RE^{3+}) ions because of their magnetic characteristics and larger ionic radii [26]. Even, a small percentage of RE^{3+} substitution can alter the magnetic and electrical properties of ferrites [27].

Herein we report structural and magnetic properties of the $La_{0.1}Co_xZn_{1.0-x}Fe_{1.9-y}Al_yO_4$, ($x = y = 0.1$ to 0.5 in steps of 0.1) synthesized by sol-gel auto-combustion method.

2. Materials and method

Nanocrystalline Co^{2+} and Al^{3+} substituted La-Zn ferrites, with composition of $La_{0.1}Co_xZn_{1.0-x}Fe_{1.9-y}Al_yO_4$ were synthesized by the sol-gel auto-combustion method [6, 19] corresponding from analytical grade reagent having purity 99%, those were Lanthanum nitrate [$La(NO_3)_3{\cdot}6H_2O$], Cobalt nitrate [$Co(NO_3)_2.6H_2O$,], Zinc nitrate [$Zn(NO_3)_2{\cdot}6H_2O$], Aluminum Nitrate [$Cr(NO_3)_3.6H_2O$], Ferric nitrate [$Fe(NO_3)_3{\cdot}9H_2O$] and 97% Glycine [NH_2-CH_2-COOH], were used in the synthesis without any further treatment. All nitrates were dissolved in distilled water to obtain a mixed solution in desired composition. The reaction procedure was carried out in an air atmosphere without the protection of inert gases. The molar ratio of metal nitrates to glycine was 1:3. The metal nitrates were dissolved together in the minimum amount of double-distilled water required to obtain a clear solution. An aqueous solution of glycine was mixed with the metal-nitrate solution and pH $\cong$7 of reaction mixture was maintained by gradually addition of the ammonia solution. The mixed solution was kept on a hot plate with constant stirring at 90 °C. A viscous brown gel was formed as a result of evaporation of solution. When all of the water molecules were evaporated; the viscous gel obtained and it began to froth, after few a minute, the gel self ignited and burnt with glowing flints. The auto-combustion completed within a short time, yielding brown colored ashes referred as the precursor.

The thermal analysis of synthesized precursors was performed using TGA/DSC Thermal analyzer SDT Q 600 V20.9 Build 20, by heating precursors from room temperature to 800 °C with a heating rate 10 °C per minutes in air atmosphere. The crystallographic structures were identified by X-ray powder diffraction with Cu Kα radiation ($\lambda = 1.5405$ Å) by Phillips X-ray diffractometer (Model 3710). Morphology and structure of the samples were studied on JEOL-JSM-5600 N scanning electron microscope (SEM) and on Philips (model CM 200) transmission electron microscope (TEM). The elemental composition determined by energy dispersive x-ray analysis (EDAX, Inca Oxford, attached to the SEM). The infrared spectra of all the samples were recorded at room

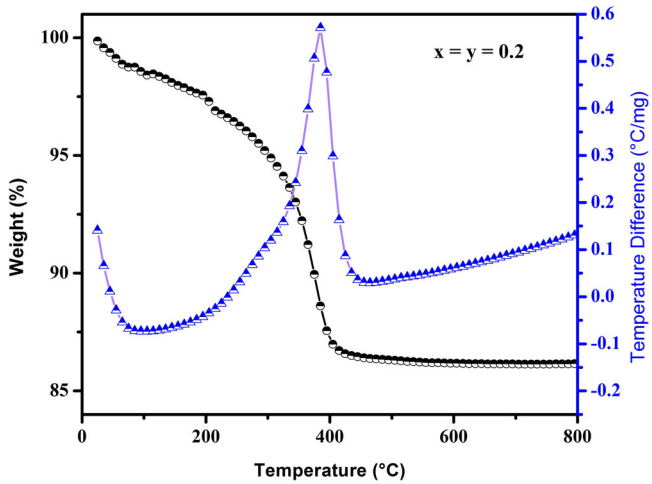

Figure 1. Typical TGA/DTA plot of $La_{0.1}Co_xZn_{1.0-x}Fe_{1.9-y}Al_yO_4$ (x = y = 0.2).

temperature in the range 200 to 800 cm^{-1} using Perkin Elmer infrared spectrophotometer. The magnetic measurements were performed at room temperature using a commercial PARC EG&G VSM 4500 vibrating sample magnetometer.

3. Result and discussion

3.1. TGA/DTA analysis

The typical decomposition pattern of Co^{2+} and Al^{3+} substituted La-Zn ferrites (x = y = 0.2) precursor is shown in Figure 1, indicate the first endothermic peak is observed due to loss of co-ordinated water molecule. Above temperature 350 °C there is mass loss which may be related to solid state an exothermic reaction results in formation of ferro-spinel compounds. The other precursors of series show similar type of decomposition patterns and convert in to ferrites in the temperature around 450 °C. Finally all precursors were calcinated at 450 °C for 4 hours to get desired nano ferro- spinels.

3.2. Elemental analysis

Energy dispersive X-ray analysis (EDAX) was obtained to investigate the elemental stoichiometric composition of the prepared La-Zn ferrite samples with Co^{2+} and Al^{3+} substitutions. EDAX of a typical samples (x = y = 0.2 and 0.4) are shown in by Figure 2a and 2b respectively. The theoretical and observed atomic elemental compositions are graphically illustrated in Figure 3. The observed elemental analysis obtained by EDAX is analogues with the theoretical compositions used for the preparation.

3.3. Structural analysis

The XRD patterns of calcinated samples is shown in Figure 4. The XRD patterns showed the appropriate peaks to the Co^{2+} and Al^{3+} substituted La-Zn ferrites and with

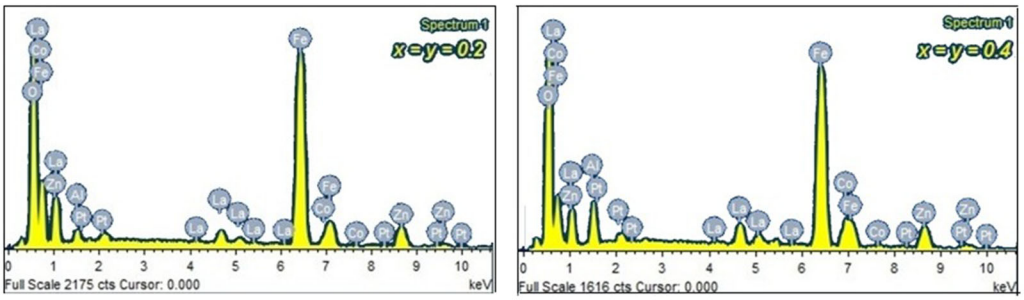

(a) (b)

Figure 2. (a) Typical EDAX pattern of $La_{0.1}Co_xZn_{1.0-x}Fe_{1.9-y}Al_yO_4$ (x = y = 0.2). (b) Typical EDAX pattern of $La_{0.1}Co_xZn_{1.0-x}Fe_{1.9-y}Al_yO_4$ (x = y = 0.4).

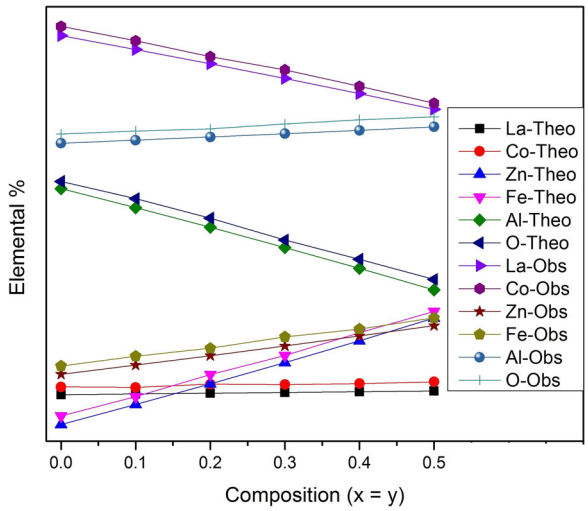

Figure 3. Plots of Observed and Theoretical elemental % versus composition (x = y).

some secondary phases. The secondary phase detected is corresponding to the ortho-ferrite phase of $LaFeO_3$ (JCPDS # 75-0541) [28].

The lattice constant 'a' was calculated by using Eq. (1) [29],

$$a = d\sqrt{N} \tag{1}$$

Where, 'a' is lattice constant, 'd' is interplaner spacing and $\sqrt{N} = \sqrt{(h^2 + k^2 + l^2)}$. The lattice constant 'a' decreased from 8.4388 Å to 8.3226 Å with the Co^{2+} and Al^{3+} ions substitution to the La-Zn ferrite system (Table 1), which is related to the ionic radii of respective ions in the composition where smaller Co^{2+} (0.65 Å) ions was substituted for the larger Zn^{2+} (0.74 Å) ions [30] and smaller Al^{3+} (0.50 Å) substituted for the larger Fe^{3+} (0.67 Å) ions [15].

The X-ray density 'd_x' was obtained by using the following relation:

$$d_x = \frac{nM}{N_A V} \tag{2}$$

Where, d_x = X-ray density, n = Number of molecules per unit volume (8 for cubic

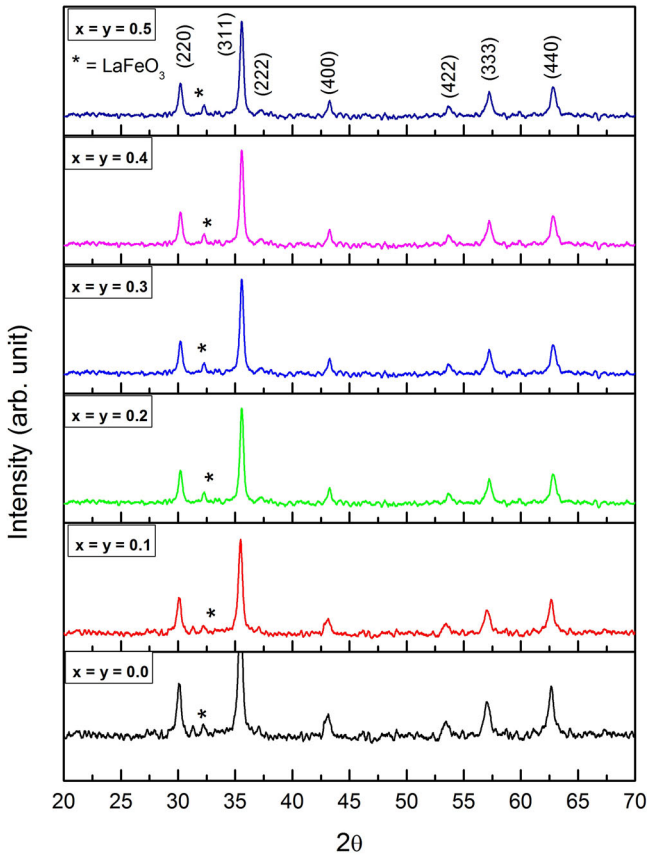

Figure 4. XRD patterns of $La_{0.1}Co_xZn_{1.0-x}Fe_{1.9-y}Al_yO_4$ (x = y = 0.0 to 0.5).

Table 1. Lattice parameter 'a', X-ray density 'd_x', particle size 'D_{XRD}', hopping lengths L_A and L_B.

Comp. x = y	A (Å)	dx (g/cm^3)	D_{XRD} (nm) XRD	D_{XRD} (nm) TEM	Hopping lengths L_A (Å)	Hopping lengths L_A (Å)
0.0	8.4388	5.5121	23.994	25.362	3.6541	2.9836
0.1	8.4170	5.4762	21.869	22.951	3.6447	2.9759
0.2	8.3891	5.4516	20.340	21.574	3.6326	2.9660
0.3	8.3626	5.4233	18.306	19.061	3.6211	2.9566
0.4	8.3505	5.3664	15.688	17.832	3.6159	2.9523
0.5	8.3226	5.3392	14.448	16.870	3.6038	2.9425

structure), M = Molecular weight of the composition, N_A = Avogadro's number = 6.02214×10^{23} and V = Volume = a^3. X-ray density decreased with Co^{2+} and Al^{3+} substitution from 5.5121 to 5.3392 g/cm^3 (Table 1).

The broad diffraction peaks exhibit the fine particle nature of synthesized ferrite samples. The average crystalline size 'D_{XRD}' of the prepared samples was determined from the most intense peak (311) plane of XRD and by using following Scherer relation [31].

$$D_{XRD} = \frac{k\lambda}{\beta \operatorname{Cos} \theta_B} \quad 3)$$

Table 2. Cation distribution over tetrahedral A and octahedral B sites and Ionic radii of tetrahedral A-site (r_A), octahedral B-site (r_B), theoretical lattice constant (a_{th}) and oxygen positional parameter (u).

	Cation distribution					
Comp. x = y	A site	B site	r_A (Å)	r_B (Å)	a_{th} (Å)	U (Å)
0	$(Zn_{1.0})$	$(La_{0.1}Fe_{1.9})$	0.7400	0.6634	8.4606	0.3906
0.1	$(Zn_{0.9}Fe_{0.1})$	$(La_{0.1}Co_{0.1}Fe_{1.7}Al_{0.1})$	0.7305	0.6616	8.4412	0.3902
0.2	$(Zn_{0.8}Fe_{0.2})$	$(La_{0.1}Co_{0.2}Fe_{1.5}Al_{0.2})$	0.7210	0.6598	8.4218	0.3899
0.3	$(Zn_{0.7}Fe_{0.3})$	$(La_{0.1}Co_{0.3}Fe_{1.3}Al_{0.3})$	0.7115	0.6580	8.4024	0.3896
0.4	$(Zn_{0.6}Fe_{0.4})$	$(La_{0.1}Co_{0.4}Fe_{1.1}Al_{0.4})$	0.7020	0.6562	8.3829	0.3893
0.5	$(Zn_{0.5}Fe_{0.5})$	$(La_{0.1}Co_{0.5}Fe_{0.9}Al_{0.5})$	0.6925	0.6544	8.3635	0.3889

Where, D = Particle Size, k = Constant (0.94), λ = Wavelength of incident X-rays, β = Full Width of Half Maxima (FWHM in radians) or broadening of the diffraction peak and θ_B = Bragg's angle. The calculated crystalline size are of the order few nm and is tabulated in Table 1. The crystalline size decreased from 23.994 to 14.448 nm with the Co^{2+} and Al^{3+} substitution.

The hopping lengths of A and B-sites (L_A and L_B, respectively) among the magnetic ions are obtained through the equation discussed elsewhere [32],

$$L_A = \frac{a\sqrt{3}}{4} \quad 4)$$

$$L_B = \frac{a\sqrt{2}}{4} \quad 5)$$

Where, 'a' is lattice constant.

It has been illustrated from Table 1 that the hopping lengths (L_A and L_B) decreased with increasing Co^{2+} and Al^{3+}concentration. The decrease in both the hopping lengths with increasing Co^{2+} and Al^{3+} substitution is due to the decrease in lattice constant. The cobalt and aluminum ions that occupy the B-sites will cause an increase in both A–A and A–B interactions and will reduce the B–B interaction. This can be ascribed to the transfer of Fe ions from B-sites to A-sites due to the insertion of both Co^{2+} and Al^{3+} ions to the B-sites. Moreover, the increase of Co^{2+} ions in the composition due to increase of x is associated with a decrease of Zn^{2+} ions. The Al^{3+} substitution to the Fe^{3+} ion difference between ionic radii of the substituted ions that brought the magnetic ions closer to each other with the decrease in hopping lengths [25].

3.4. Cation distribution

The cation distribution of the available tetrahedral and octahedral sites in spinel ferrite composition was obtained (Table 2) through the analysis of the X-ray diffraction patterns where the Bertaut method [33].

The Zn^{2+} ions showed preference to occupy the tetrahedral A sub lattice and La^{3+}, Co^{2+}, Al^{3+} ions mainly go into octahedron B sub lattice [34]. However, Fe^{3+} ions occupied both the available A and B sub lattices. Higher fraction of Co^{2+} ions occupied the B-site due to their tendency for large octahedral site energy. The fraction Co^{2+} ions at B-site increased at the cost of Fe^{3+} ions with the substitution of Co^{2+} ions. The Al^{3+} replaced the Fe^{3+} from B-sites due to their preference to the B-site and favorable crystal

Table 3. Band position (ν_1 and ν_2), force constants K_0, K_t and bond lengths R_A, R_B.

	Band position		Force constant		Bond length	
Comp. x = y	ν_1 (cm^{-1})	ν_2 (cm^{-1})	$K_0 \times 10^5$ (dyne/cm)	$K_t \times 10^5$ (dyne/cm)	R_A (Å)	R_B (Å)
0	561.97	398.78	1.0067	1.7235	0.3840	0.3057
0.1	564.37	401.78	1.0169	1.7370	0.3829	0.3053
0.2	576.89	404.31	1.0246	1.7524	0.3817	0.3048
0.3	595.03	412.86	1.0628	1.8182	0.3805	0.3044
0.4	592.63	417.24	1.0798	1.8386	0.3794	0.3039
0.5	587.027	446.823	1.1969	2.0205	0.3819	0.3049

field effects [35]. The percentage of Al^{3+} ions whereas the fraction of Fe^{3+} ions in B-sites decreased linearly with the increasing Al^{3+} content. The ionic radii of the constituent ions such as Al^{3+} (0.50 Å), Zn^{2+} (0.81 Å), Co^{2+} (0.72 Å) and Fe^{3+} (0.67 Å) may also govern the site occupancies in spinel ferrite system [36].

The oxygen positional parameters (u), experimental lattice constants (a_{exp}), the relative intensities of experimental and calculated XRD peaks (I_{hkl}) and cation distribution for each composition are tabulated in Table 3. The mean ionic radius of the A and B-sites (r_A and r_B respectively) was obtained through the relations discussed elsewhere [37]. It is observed that radius of A-site 'r_A' decreased and radius of B-site 'r_B' increased with increasing Co^{2+}concentration (Table 3). The increase in r_B is related to the occupancy of B site by the smaller Co^{2+} (0.72 Å) ions that replaced Zn^{2+} (0.74 Å) ions [38].

3.5. Infrared spectroscopy

IR spectra for all the synthesized ferrite samples are showed in Figure 5. The spectrum showed two major absorption bands ($\nu_1$and ν_2) which is an important characteristic of all the ferrites, near 600 and 400 cm^{-1} (Table 3). The high frequency band (ν_1) is allocated to the intrinsic lattice vibration of the tetrahedral sites of Fe^{3+}–O^{2-}. On the other hand, the lower frequency band (ν_2) is ascribed to the stretching vibration of octahedral complexes [39]. The calculated values bond lengths for A-site (R_A) and B-site (R_B) are listed in Table 4. The bond lengths R_A and R_B decreased with Co^{2+} and Al^{3+} substitution. The force constants K_t and K_O increased with the Co^{2+} and Al^{3+} substitution.

3.6. Scanning electron microscopy

Typical SEM micrograph of the prepared ferrites (x = y = 0.0) shown in Figure 6. SEM images indicate formation of well defined nanoparticles with slight agglomeration of the sample with inhomogeneous broader grain size distribution. It is observed from SEM images that the morphology was affected by the Co^{2+} and Al^{3+} substitutions. The SEM images showed the amorphous and porous in nature of the prepared samples. The reduction in the grain size and increment in porosity is observed with the Co^{2+} and Al^{3+} substitutions. Such observations suggested that the substitution of Co^{2+} and Al^{3+} in La-Zn ferrite during sol-gel combustion process enabled a better homogeneousness in the samples and, thus, a more precise microstructure is attained.

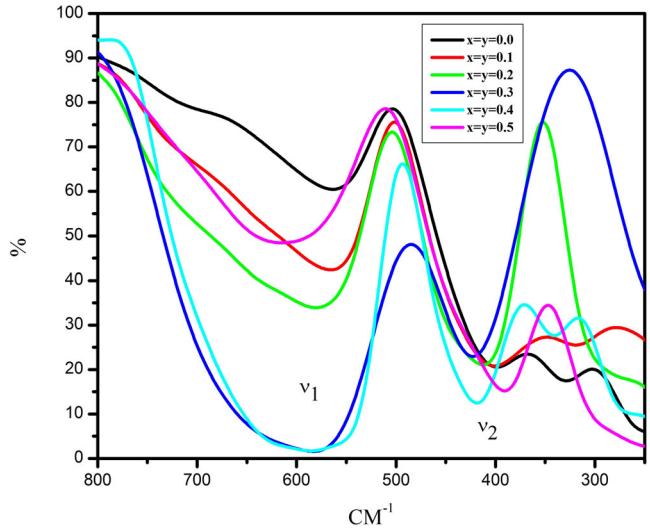

Figure 5. IR spectrum of $La_{0.1}Co_xZn_{1.0-x}Fe_{1.9-y}Al_yO_4$ (x = y = 0.0 to 0.5).

Table 4. Values of molecular weight, saturation magnetization, Remnant magnetization, coercivity and magneton number.

Comp. x = y	Ms (emu/gm)	Mr (emu/gm)	Hc (Oe)	$n_{B\ obs}$ (μ_B)
0	32.3102	8.2117	180.85	1.443
0.1	25.7482	6.9645	399.00	1.133
0.2	19.1084	4.6736	578.70	0.829
0.3	13.8681	3.6571	540.50	0.593
0.4	13.6769	3.5452	589.90	0.576
0.5	12.0344	3.1695	811.20	0.499

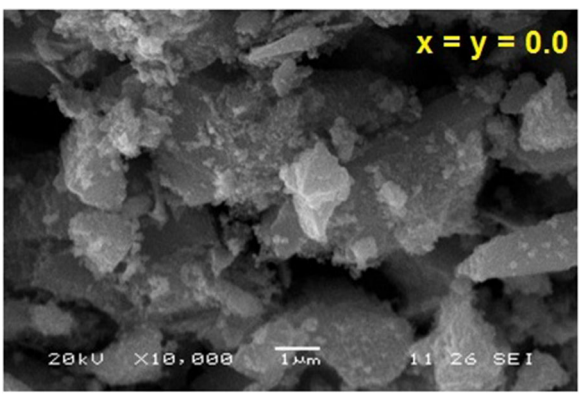

Figure 6. Typical scanning electron micrographs of $La_{0.1}Co_xZn_{1.0-x}Fe_{1.9-y}Al_yO_4$ (x = y = 0.0).

3.7. Transmission electron microscopy

Figure 7 shows the typical TEM image and their respective histogram (Figure 8) of the sample (x = y = 0.0). The values of the particle size obtained from TEM analysis are around 24–16 nm and these values are good agreements with the values are determined from XRD. Most of the spherical shaped nanoparticles has been observed, at the same

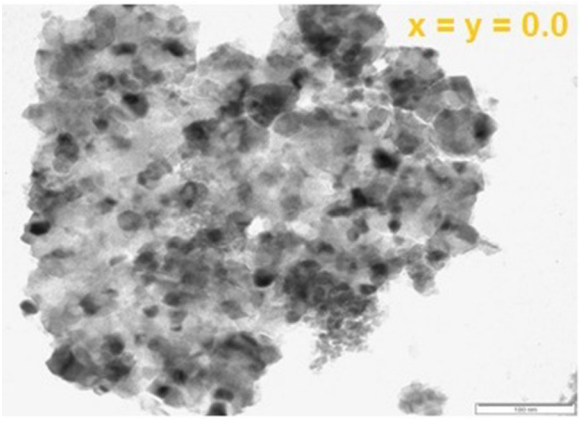

Figure 7. Typical transmission electron micrograph of $La_{0.1}Co_xZn_{1.0\text{-}x}Fe_{1.9\text{-}y}Al_yO_4$ (x = y = 0.0).

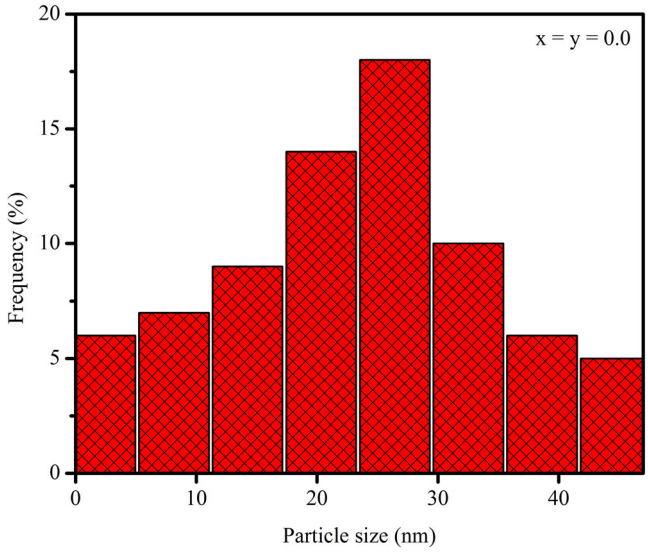

Figure 8. Particle size distribution graph of $La_{0.1}Co_xZn_{1.0\text{-}x}Fe_{1.9\text{-}y}Al_yO_4$ (x = y = 0.0).

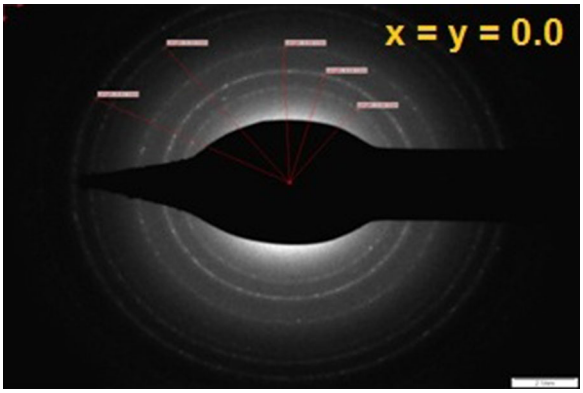

Figure 9. SAED pattern of $La_{0.1}Co_xZn_{1.0\text{-}x}Fe_{1.9\text{-}y}Al_yO_4$ (x = y = 0.0).

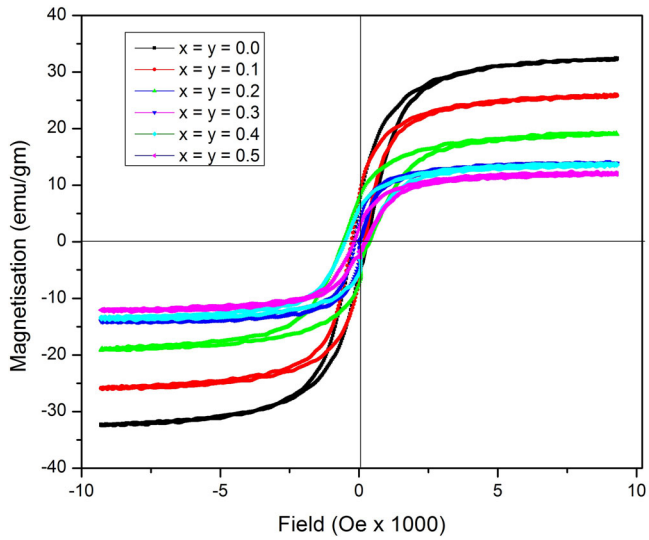

Figure 10. Hysteresis loops of $La_{0.1}Co_xZn_{1.0-x}Fe_{1.9-y}Al_yO_4$ (x = y = 0.0 to 0.5).

time, few elongated shaped agglomerated nano-particles were also evidenced due to magnetic interaction among the particles.

Figure 9 showed typical selected area electron diffraction (SAED) pattern of the (x = y = 0.0) sample. The Debye ring pattern with superimposition of the bright spot indicates poly-crystalline nature of the prepared sample [31].

3.8. Magnetization

Magnetic properties of ferrites are sensitively dependent on the structure, composition, defects, crystallite size; internal strain and cation distribution [40]. Neel's two sub-lattice models are applied to understand the magnetic behavior of the samples. According to Neel's two sub-lattice Model of ferrimagnetism Neel's magnetic moment n_B is given by equation [41]. The super-exchange interactions of these samples strongly depend on the distribution of the cations on the tetrahedral, A- and the octahedral, B-site.

It is observed from Fig. 9, that saturation magnetization decreases up to certain applied field above which saturation magnetization remains almost constant. Saturation magnetization (Ms), coercivity (Hc), and magneton number (n_B) derived from hysteresis loops and are given in Table 4. Saturation magnetization decreases from 36.546 emu/g to 3.397 emu/g, with increase in Co^{2+} and Al^{3+} content. Remnant magnetization (Mr) obtained from the hysteresis loop is observed to decreased with the increase in Co^{2+} and Al^{3+} substitution. The increases in coercivity could also be related to the higher magneto crystalline anisotropy of Co^{2+} ions as compared to the Fe^{3+} ions.

It is illustrated in Figure 10, that saturation magnetization (Ms) increased up to specific applied magnetic field above which Ms attains a saturated moment. Ms, coercivity (Hc), and magneton number (n_B) was derived from hysteresis loops and are tabulated in Table 4. Saturation magnetization decreases from 32.3102 emu/g to 12.0344 emu/g, with increase in Co^{2+} and Al^{3+} content. Remnant magnetization (Mr) observed from the hysteresis loop is decreased with the Co^{2+} and Al^{3+}substitution. The increase in

coercivity should be related to the higher magneto crystalline anisotropy of Co^{2+} ions as compared to the Fe^{3+} ions.

The observed magneton number n_B (the Ms per formula unit in μ_B) was determined by hysteresis loops. The net magnetic moment (n_BCal.) can be obtained from the sum of the magnetic moments at A and B sub lattices, i.e., n_BCal. = M_B-M_A; where, M_B and M_A are the B and A sub-lattice magnetic moments in μ_B. The n_B Cal. were obtained through cation distribution and magnetic moments of Fe^{3+} (5.92μ_B), Al^{3+} (0μ_B), Zn^{2+} (0μ_B), Co^{2+} (3.88 μ_B) and La^{3+} (3.58 μ_B). Magneton number decreased with Co^{2+} and Al^{3+} substitution (Table 4).

4. Conclusions

Nanocrystalline ferrites, with composition $La_{0.1}Co_xZn_{1-x}Fe_{1.9-y}Al_yO_4$ in step of x = y = 0.1, 0.2, 0.3, 0.4 and 0.5 were successfully prepared by the sol-gel auto-combustion method. All precursors were calcined at 450 °C for four hour. The observed elemental analysis from EDAX is in good agreement with the theoretical values. The lattice constant decreased from 8.4388 Å to 8.3226 Å, and the crystalline size decreased from 23.994 nm to 14.448 nm with the Co^{2+} and Al^{3+} ions substitution. Zn^{2+} ions prefer to occupy the tetrahedron site (A sub lattice) and both La^{3+}, Co^{2+}, Al^{3+} ions mainly enter octahedron site (B sub lattice). The I.R. spectra showed two principle absorption bands ($\nu_1$and ν_2) near 600 and 400 cm^{-1} which is a characteristic feature of spine ferrites and supported the XRD investigations. SEM and TEM images revealed well defined nanoparticles with slight agglomeration. Magneton number decreased with Co^{2+} and Al^{3+} substitution.

ORCID

U. M. Mandle http://orcid.org/0000-0002-7308-7720
K. S. Lohar http://orcid.org/0000-0003-1933-2542
B. L. Shinde http://orcid.org/0000-0001-6568-5977

References

[1] R. Jasrotia *et al.*, Synthesis and characterization of Mg-Ag-Mn nano-ferrites for electromagnet applications, *Phys. B Condens. Matter.* **569**, 1 (2019). DOI: 10.1016/j.physb.2019.05.033.

[2] K. K. Kefeni, B. B. Mamba, and T. A. Msagati, Application of spinel ferrite nanoparticles in water and wastewater treatment: a review, *Sep. Purif. Technol.* **188**, 399 (2017). DOI: 10.1016/j.seppur.2017.07.015.

[3] K. A. Ganure *et al.*, Synthesis, structural and magnetic properties of Ni^{2+} and In^{3+} doped cobalt ferrite and application as catalyst for synthesis of Bis-(Indolyl) methane derivatives, *Mater. Today: Proc.* (2021). DOI: 10.1016/j.matpr.2021.02.327.

[4] C. A. P. Gómez *et al.*, Structural parameters and cation distributions in solid state synthesized Ni-Zn ferrites, *Mater. Sci. Eng, B.* **236**, 48 (2018). DOI: 10.1016/j.mseb.2018.12.003.

[5] H. Yang *et al.*, A simple gas sensor based on zinc ferrite hollow spheres: Highly sensitivity, excellent selectivity and long-term stability, *Sens. Actuators, B.* **280**, 34 (2019). DOI: 10.1016/j.snb.2018.10.056.

[6] U. M. Mandle *et al.*, An efficient one pot multicomponent synthesis of pyrano pyrazoles using Cu^{2+} doped Ni-Zn nano ferrite catalyst, *Mater. Today: Proc.* **46**, 6122 (2021)., DOI: 10.1016/j.matpr.2020.03.583.

[7] T. Rahman, G. Borah, and P. K. Gogoi, Spinel structured copper ferrite nano catalyst with magnetic recyclability for oxidative decarboxylation of phenyl acetic acids, *Catal. Lett.* **150** (8), 2267 (2020). DOI: 10.1007/s10562-020-03131-0.

[8] N. L. Martínez-Rodríguez *et al.*, In vitro toxicity assessment of zinc and nickel ferrite nanoparticles in human erythrocytes and peripheral blood mononuclear cell, *Toxicol. In Vitro* **57**, 54 (2019). DOI: 10.1016/j.tiv.2019.02.011.

[9] Y. Du *et al.*, Optimization and design of magnetic ferrite nanoparticles with uniform tumor distribution for highly sensitive MRI/MPI performance and improved magnetic hyperthermia therapy, *Nano Lett.* **19** (6), 3618 (2019). DOI: 10.1021/acs.nanolett.9b00630.

[10] A. Nigam, and S. J. Pawar, Structural, magnetic, and antimicrobial properties of zinc doped magnesium ferrite for drug delivery applications, *Ceram. Int.* **46** (4), 4058 (2020). DOI: 10.1016/j.ceramint.2019.10.243.

[11] V. K. Chakradhary, A. Ansari, and M. J. Akhtar, Design, synthesis, and testing of high coercivity cobalt doped nickel ferrite nanoparticles for magnetic applications, *J. Magn. Magn.* **469**, 674 (2019). DOI: 10.1016/j.jmmm.2018.09.021.

[12] I. H. Hasan *et al.*, Nickel zinc ferrite thick film with linseed oil as organic vehicle for microwave device applications, *Mater. Chem. Phys.* **236**, 121790 (2019). DOI: 10.1016/j.matchemphys.2019.121790.

[13] W. I. Liu *et al.*, Impact of oscillating magnetic field on the thermal-conductivity of water-Fe_3O_4 and water-Fe_3O_4/CNT ferro-fluids: experimental study, *J. Magn. Magn.* **484**, 258 (2019). DOI: 10.1016/j.jmmm.2019.04.042.

[14] G. S. Kumar, and A. R. Synthesis, structural, dielectric and magnetic properties of spinel structure of Ca^{2+} substitute in Cobalt ferrites ($Co_{1-x}Ca_xFe_2O_4$), *Chin. J. Phys.* **56** (3), 1262 (2018). DOI: 10.1016/j.cjph.2018.02.014.

[15] B. L. Shinde *et al.*, Synthesis and characterization of Al^{3+} substituted Ni–Cu–Zn nano ferrites, *J. Therm. Anal. Calorim.* (2021). DOI: 10.1007/s10973-021-10719-0.

[16] K. Jalaiah, and K. V. Babu, Structural, magnetic and electrical properties of nickel doped Mn-Zn spinel ferrite synthesized by sol-gel method, *J. Magn. Magn.* **423**, 275 (2017). DOI: 10.1016/j.jmmm.2016.09.114.

[17] M. Li *et al.*, Synthesis and characterization of nanosized MnZn ferrites via a modified hydrothermal method, *J. Magn. Magn.* **439**, 228 (2017). DOI: 10.1016/j.jmmm.2017.04.015.

[18] W. Chen *et al.*, Structural and magnetic properties evolution of Co-Nd substituted M-type hexagonal strontium ferrites synthesized by ball-milling-assisted ceramic process, *J. Elect. Mater.* **47** (3), 2110 (2018). DOI: 10.1007/s11664-017-6021-8.

[19] B. L. Shinde *et al.*, Preparation and characterization of chromium doped Ni-Cu-Zn nano ferrites, *Acta Chim Slov.* **64** (4), 931 (2017). DOI: 10.17344/acsi.2017.3619.

[20] M. Hashim *et al.*, Manganese ferrite prepared using reverse micelle process: structural and magnetic properties characterization, *J. Alloys Compd.* **642**, 70 (2015). DOI: 10.1016/j.jallcom.2015.04.085.

[21] M. K. Anupama, B. Rudraswamy, and N. Dhananjaya, Influence of trivalent (Gd^{3+}, Cr^{3+}) ion substitution on the structural and magnetic properties of $Ni_{0.4}Zn_{0.6}Cr_{0.5}Gd_xFe_{1.5-x}O_4$ ferrite nanoparticles, *IJNT* **14** (9/10/11), 867 (2017). DOI: 10.1504/IJNT.2017.086770.

[22] M. Z. Khan *et al.*, Comprehensive study on structural, electrical, magnetic and photocatalytic degradation properties of Al^{3+} ions substituted nickel ferrites nanoparticles, *J. Alloys Compd.* **848**, 155795 (2020). DOI: 10.1016/j.jallcom.2020.155795.

[23] V. K. Mande *et al.*, Effect of Zn^{2+}-Cr^{3+} substitution on structural, morphological, magnetic and electrical properties of $NiFe_2O_4$ ferrite nanoparticles, *J. Mater. Sci: Mater. Electron.* **29** (17), 15259 (2018). DOI: 10.1007/s10854-018-9668-x.

[24] T. K. Bromho *et al.*, Understanding the impacts of Al^{3+}-substitutions on the enhancement of magnetic, dielectric and electrical behaviors of ceramic processed nickel-zinc mixed

ferrites: FTIR assisted studies, *Mater. Res. Bull.* **97**, 444 (2018). DOI: 10.1016/j.materresbull.2017.09.013.

[25] H. M. Zaki, S. H. Al-Heniti, and M. M. Aljwiher, Synthesis, structural, magnetic and dielectric studies of aluminum substituted cobalt-copper ferrite, *Physica B: Condens. Matter.* **597**, 412382 (2020). DOI: 10.1016/j.physb.2020.412382.

[26] K. L. Routray, S. Saha, and D. Behera, Rare-earth (La^{3+}) substitution induced changes in the structural, dielectric and magnetic properties of nano-$CoFe_2O_4$ for high-frequency and magneto-recording devices, *Appl. Phys. A.* **125** (5), 1 (2019). DOI: 10.1007/s00339-019-2615-8.

[27] S. M. Kabbur *et al.*, Magnetic interactions and electrical properties of Tb^{3+} substituted NiCuZn ferrites, *J. Magn. Magn.* **473**, 99 (2019). DOI: 10.1016/j.jmmm.2018.10.041.

[28] K. A. Ganure *et al.*, Influence of La^{3+} doped nano spinel ferrites on infrared spectroscopy in elastic properties via O/W micro emulsion method, *Ferroelectrics* **573** (1), 236 (2021). DOI: 10.1080/00150193.2021.1890480.

[29] S. G. Gawas, and V. M. S. Verenkar, Precursor combustion synthesis of nanocrystalline cobalt substituted nickel zinc ferrites from hydrazinated mixed metal fumarates, *Thermochim. Acta* **605**, 16 (2015). DOI: 10.1016/j.tca.2015.02.010.

[30] T. R. Tatarchuk *et al.*, Structural characterization and antistructure modeling of cobalt-substituted zinc ferrites, *J. Alloys Compd.* **694**, 777 (2017). DOI: 10.1016/j.jallcom.2016.10.067.

[31] B. D. Cullity, *Elements of X-Ray Diffraction* (Addison-Wesley Publ. Comp. Inc., Reading, MA, 1956), p. 99.

[32] M. V. Chaudhari *et al.*, Combustion synthesis of Co^{2+} substituted $Li_{0.5}Cr_{0.5}Fe_2O_4$ nano-powder: Physical and magnetic interactions, *Powder Technol.* **259**, 14 (2014). DOI: 10.1016/j.powtec.2014.03.053.

[33] L. Weil, F. Bertaut, and L. Bochirol, Propriétés magnétiques et structure de la phase quadratique du ferrite de cuivre, *J. Phys. Radium* **11** (5), 208 (1950). DOI: 10.1051/jphysrad:01950001105020800.

[34] M. Han, C. R. Vestal, and Z. J. Zhang, Quantum couplings and magnetic properties of CoCr x Fe2-x O4 (0< x< 1) spinel ferrite nanoparticles synthesized with reverse micelle method, *J. Phys. Chem. B.* **108**, 583 (2004). DOI: 10.1021/jp035966m.

[35] H. M. Widatallah *et al.*, On the synthesis and cation distribution of aluminum-substituted spinel-related lithium ferrite, *Mater. Lett.* **59** (8–9), 1105 (2005). DOI: 10.1016/j.matlet.2004.12.017.

[36] L. Vegard, The constitution of the solid solution and the space filling of the atoms, *Z. Physik.* **5** (1), 17 (1921). DOI: 10.1007/BF01349680.

[37] K. J. Standley, *Oxide Magnetic Materials* (Oxford University Press, Oxford, UK, 1972).

[38] U. B. Shinde *et al.*, Preparation and characterization of Co2+ substituted Li–Dy ferrite ceramics, *Ceram. Int.* **39** (5), 5227 (2013). DOI: 10.1016/j.ceramint.2012.12.022.

[39] R. D. Waldron, Preparation of magnetic nanoparticles, *Phys. Rev.* **99** (6), 1727 (1955). DOI: 10.1103/PhysRev.99.1727.

[40] L. Z. Li *et al.*, Structural and magnetic properties of Cr-substituted NiZnCo ferrite nano-powders, *J. Magn. Magn.* **381**, 328 (2015). DOI: 10.1016/j.jmmm.2015.01.020.

[41] L. Néel, Propriétés magnétiques des ferrites; ferrimagnétisme et antiferromagnétisme, *Ann. Phys.* **12** (3), 137 (1948). DOI: 10.1051/anphys/194812030137.